Multiscale modeling of freeze-thaw behavior in granular media

Shiwei Zhao[1], Hao Chen[2], and Jidong Zhao[1,3*]

[1]*Department of Civil and Environmental Engineering, Hong Kong University of Science and Technology (HKUST), Hong Kong 999077, China;*
[2]*State Key Laboratory of Subtropical Building Science, South China University of Technology, Guangzhou 510641, China;*
[3]*HKUST Shenzhen-Hong Kong Collaborative Innovation Research Institute, Shenzhen 518045, China*

This paper presents a hierarchical multiscale modeling paradigm to simulate the freeze-thaw behavior in granular media. The multiscale strategy features a hierarchical conjugate of a continuum-based mixture theory with a micromechanics-based homogenization technique. It enables the capturing of a typical freeze-thaw process in an engineering setting based on constitutive responses extracted directly from discrete element method (DEM) solution of representative volume elements (RVEs) affiliated with material points. Specifically, at the RVE scale, a simple phase transition model is proposed to consider the influence of freeze-thaw process on the strength of inter-particle contacts. The RVE model is further embedded in the material point of the continuum-based material point method (MPM) to solve initial and boundary value problems that involve freeze and thaw process. The proposed strategy effectively enables macro-micro scale bridging while bypassing the necessity of assuming phenomenological thermo-mechanical constitutive models. The multiscale framework is verified and validated before being used to predict engineering-scale thawing-induced slides of soils.

Multiscale modeling, Granular media, Freeze-thaw, Discrete element, Material point method

1. Introduction

Granular media are ubiquitous in nature and our daily life. They are the second most processed material after water in the world. Granular materials are typical porous media. Their inter-particle pores are frequently partially or fully filled with fluids and/or other pore-filling materials (typically air, water and/or ice or gas hydrate). If the pore-filling materials are thermal sensitive and may undergo phase transition, temperature changes may induce freezing and thawing for the material. Such freezing and thawing processes are expected to influence the bulk mechanical properties of granular media significantly, thereby triggering large deformation or even rapid flow that may cause catastrophic failures such as landslides and debris flows. For example, due to global warming, thawing occurs continuously across large-

area permafrost (one of the world's largest carbon sinks) including Northern Europe, Iceland, Greenland, the European Alps, Alaska, Siberia, northeastern China, the Tibetan Plateau, South America and the Antarctic Peninsula [1], resulting in numerous hazardous landslides accompanied with significant carbon release into the atmosphere [2]. Beyond the natural freezing and thawing, it is also of importance to model and examine the freeze-thaw behaviors of granular media in industry and engineering practices. Taking the gas hydrate exploitation as an example, the dissociation of gas hydrates can remarkably weaken the host sediment due to the loss of inter-particle cementation, thereby causing excessive deformation in the host sediment and its overlying strata and triggering potential geohazards such as submarine landslides, earthquakes and even tsunamis, considerably threatening offshore infrastructures and coastal cities [3].

Great efforts have been dedicated to modeling freeze-thaw behaviors of granular media, especially for frozen soils in

---

the geotechnical community [4-6]. Most of existing studies have been focused on proposing sophisticated constitutive models to capture the thermo-hydro-mechanical (THM) responses of granular media from a continuum perspective, where granular media are homogenized with mixture theory for consideration of multi-phase. These models are commonly phenomenological but are easy to be implemented in the continuum-based numerical methods such as FEM [7] for simulation of large-scale problems. However, FEM might encounter potential issues of mesh distortion and convergence for large-deformation problems. These issues can be alleviated partially by specific techniques such as mesh refinements or adaptive meshing but at the cost of computational efficiency and possible convergence [8]. As a consequence, mesh-free continuum methods, especially the material point method (MPM) [9], have received growing interests in tackling large deformation problems over past decades, e.g., hydro-mechanical coupling [10], and THM coupling [11].

Continuum-based approaches using conventional continuum constitutive models may encounter great difficulties in fully capturing complicated behaviors exhibited in granular media, such as anisotropy, non-coaxiality, loading history-dependency, and cyclic hysteresis, which limits their application in predicting the freeze-thaw response of granular media, especially for large-deformation problems. Meanwhile, discrete element method (DEM) has enjoyed an increasing popularity as a micromechanics tool to simulate complex responses of granular media. Indeed, hierarchical multiscale modeling that couples both the continuum numerical methods (e.g., FEM, MPM) and DEM has proven effective and promising to simulate engineering-scale problems involving granular media while tactically avoiding some of the pitfalls of conventional continuum modeling [12, 13]. In particular, Zhao et al. [14] recently proposed a hierarchical multiscale framework to model thermo-mechanical responses of granular media by coupling FEM and DEM where particle-scale contact heat conduction is considered. The study, however, has not been able to tackle the freezing and thawing process with explicit consideration of phase transition yet.

In this work, a new multiscale framework is proposed to model freeze-thaw behavior of granular media with full consideration of phase transition of pore-filling materials in both micro- and macro-scales. The remainder of this paper is organized as follows. Representative volume element (RVE) models of freeze-thaw process are first introduced in Sect. 2, where the continuum-based mixture theory is employed in conjunction with the micromechanics-based DEM. Then, thermo-mechanical formulation and implementation with phase transition of filling materials are proposed for the macroscopic freeze-thaw modeling in Sect. 3. Section 4 in-

troduces the coupling scheme of the proposed hierarchical mutiscale framework DEMPM, followed by verification, validation and examples of the proposed framework in Sect. 5 and a summary in Sect. 6.

2. RVE models of freeze-thaw process

2.1 Thermally-induced deformation and stress

Granular media can be regarded as mixtures of grains, ice and water/air as shown in Fig. 1. Thermally-induced deformation is dominated by volume change due to phase transition between solid (e.g., ice) and fluid (e.g., water), resulting in remarkable thermally-induced stress accordingly. By contrast, the expansion/contraction of a solid grain caused by thermal changes is negligibly small so that the corresponding thermal stress can be neglected. If phase transition is involved during freezing or thawing, in addition to volume change induced by phase transition, the variation of inter-particle cementation has a significant effect on the bulk strength of granular media such as frozen soils in permafrost areas and gas hydrate-bearing soils in submarine settings. Hence, a thermally-sensitive contact model is proposed to consider the influence of inter-particle cementation in DEM-simulated RVEs.

2.2 Mixture properties

In the theory of mixture [15], the bulk volumetric heat capacity ρc of a saturated mixture can be defined as

$$\rho c = \rho_f c_f \theta_f + \rho_s c_s \theta_s + \rho_g c_g \theta_g, \tag{1}$$

where ρ is the mass density and c is the mass heat capacity (with subscript f, s and g for fluid (water), solid (ice) and gains, respectively); θ_f, θ_s and θ_g are the corresponding volu-
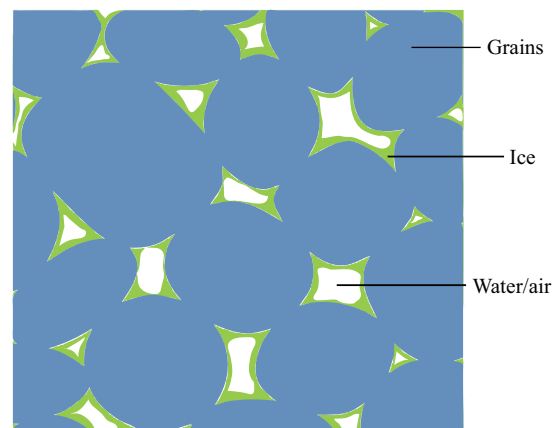
Figure 1 RVE of a granular material composed of grains, ice and water/air.

metric fractions of the three phases, respectively. The effective thermal conductivity of the mixture can be also given with respect to the three phases as [15]

$$k = k_g^{\theta_g} k_f^{\theta_f} k_s^{\theta_s}. \tag{2}$$

For simplicity, the effect of water flow is not considered so that no water flowing in/out from the RVE is assumed, and the RVE satisfies the mass conservation, i.e.,

$$\rho_f \theta_f - \rho_s \theta_s = 0. \tag{3}$$

For coarse granular materials, almost all water freezes at the freezing point, whereas temperature keeps decreasing during freezing for fine granular materials such as silt and clay [5]. The unfrozen water content w is defined as the ratio of water mass to grain mass. Hence, the volumetric fraction of ice can be given by

$$\theta_s = n - \frac{\rho_g}{\rho_f}(1 - n)w, \tag{4}$$

where n is the porosity ($= 1 - V_g/V$, with V_g and V denoting the volumes of solid grains and the bulk mixture, respectively).

2.3   Contact bond model in DEM

2.3.1   No bond

For contacted particles without connection by bonds, a force-displacement law is postulated for inter-particle contact force evaluation in conjunction with the Coulomb's friction condition [16] as below:

$$\boldsymbol{f}^n = -k_n \boldsymbol{u}^n, \tag{5a}$$

$$\Delta \boldsymbol{f}^t = -k_t \delta \boldsymbol{u}^t, \tag{5b}$$

$$|\boldsymbol{f}^t| \le \mu |\boldsymbol{f}^n|, \tag{5c}$$

where $\boldsymbol{f}^n$ and $\boldsymbol{f}^t$ are the normal and tangential contact forces at contact, respectively; $\Delta \boldsymbol{f}^t$ is the incremental tangential contact force at the current timestep; k_n and k_t are the normal and tangent contact stiffness, respectively, which are assumed to be constant for a linear spring model; $\boldsymbol{u}^n$ is the normal penetration, $\delta \boldsymbol{u}^t$ is the relative tangential displacement at the contact, and μ is the coefficient of friction.

2.3.2   Bond model

For cemented particles, the inter-particle cementation can be taken into account by introducing a contact bond [17,18]. For simplicity yet without losing generality, we introduce the following thermally sensitive bond contact model that governs the bond breakage upon heating:

$$\|\boldsymbol{f}^n\| > F_{nb}, \quad F_{nb} = \beta_b c_n \hat{r}^2, \tag{6}$$

$$\|\boldsymbol{f}^t\| > F_{tb}, \quad F_{tb} = \beta_b c_t \hat{r}^2, \tag{7}$$

where β_b is defined as the breakage strength coefficient that is associated with the volumetric fraction of ice; $\hat{r}$ is the radius of the smaller particle at contact; c_n and c_t are the normal and shear bond strength, respectively. Contact bond breaks and can no longer sustain tension once either normal or shear contact force reaches the corresponding strength. Note that bond breakage is only subject to tension and shear for simplicity, and it is optional to incorporate bond failure caused by twisting and/or compression in a more rigorous model. Note that such a simplified bond model has been successfully incorporated into our previous hierarchical multiscale modeling framework to investigate compression behavior of sandstone [19, 20].

2.3.3   Simplified phase transition model

At the RVE level, phase transition of pore water/ice is considered in such a manner that inter-particle bonds are weakened or enhanced uniformly over the entire RVE. To this end, the breakage strength coefficient β_b is introduced as a function of the volumetric fraction of ice θ_s, simply defined as

$$\beta_b = \beta_a \frac{\theta_s}{\theta_s + \theta_f}, \tag{8}$$

where β_a is a tuned parameter and θ_f is the volumetric fraction of unfrozen water. Note that the state variable θ_s is solved from heat transfer at the macroscopic continuum.

3.   Macroscopic thermo-mechanical modeling

3.1   Governing equations

For a three-phase granular mixture as shown in Fig. 1, the coupled THM effect has been taken into account in general engineering practice. However, the freeze-thaw process may complicate the problem significantly. For simplicity, no water flow is assumed within the mixture, and the energy conservation law reads

$$\rho c T_{,t} + q_{i,i} = Q_t + L\rho_s \theta_{s,t}, \tag{9}$$

where ρ is the bulk mass density of the mixture; c is the specific heat capacity; T is the temperature; t is the time; q_i is the heat flux; Q_t is a heat source or sink; L is the water latent heat of fusion per unit mass; θ_s is the volumetric fraction of ice; ρ_s is the mass density of ice. According to the Fourier's law for anisotropic heat conduction, the heat flux q_i can be written as [21]

$$q_i = -k_{ij} T_{,j}, \tag{10}$$

where k_{ij} is the thermal conductivity tensor, which can be associated with granular fabric [14]. Note that for granular media such as soils, variation of thermal conductivity due to shear-induced anisotropy is not considered.

The balance equation of linear momentum is given by

$$\sigma_{ij,j} + \rho b_i = \rho a_i, \tag{11}$$

where σ_{ij} is the Cauchy stress tensor; b_i is the body force per unit of mass possibly performed on materials (e.g., gravitational acceleration), and a_i is the acceleration term.

The following general boundary and initial conditions are considered for a typical mechanical problem involving heat conduction:

$$T(t) = \bar{T}, \text{ on } \Gamma_T, \text{ Dirichlet BC}, \tag{12a}$$

$$q(t)_i = \bar{q}_i, \text{ on } \Gamma_q, \text{ Neumann BC}, \tag{12b}$$

$$T(0) = T_{\text{ref}}, \text{ on } \Omega, \text{ initial temperature}, \tag{12c}$$

$$u_i = \bar{u}_i, \text{ on } \Gamma_u, \text{ Dirichlet BC}, \tag{12d}$$

$$\sigma_{ij} n_j = \bar{t}_i, \text{ on } \Gamma_t, \text{ Neumann BC}, \tag{12e}$$

where BC is boundary condition; Γ_T and Γ_q are the prescribed temperature and heat flux boundaries of the problem domain Ω, respectively; $\bar{T}$ and $\bar{q}_i$ are the prescribed boundary temperature on Γ_T and boundary heat flux on Γ_q, respectively; T_{ref} is the ambient or reference temperature; n_j is the boundary outward normal of the domain Ω; $\bar{u}_i$ and $\bar{t}_i$ are the prescribed material displacement on Γ_u and boundary traction on Γ_t, respectively.

3.2 Spatial discretization

The generalized interpolation material point (GIMP) formulation [9] in MPM is employed to discretize the macroscopic continuum into a finite set of subdomains, where each material point has a certain domain. Specifically, the undeformed GIMP (uGIMP) [9] is adopted here for simplicity in implementation without losing generality. The weak forms of the governing equations have integration over the entire domain Ω, which can be converted into the summation of integration over each subdomain Ω_p of particles in MPM.

In MPM, a physical field f_p or $g(x_i)$ can be interpolated based on either material points or grid nodes as follows:

$$f(x_i) = \sum_p f_p \chi_p(x_i), \tag{13}$$

$$g(x_i) = \sum_I g_I N_I(x_i), \tag{14}$$

where $\chi_p(x_i)$ is the particle characteristic function, satisfying the partition of unity property in the undeformed configuration and a "top-hat" function is employed here; $N_I(x_i)$ is the grid shape function at node I; the subscripts p or I denote

properties or functions associated with particle p or node I hereafter. For example, the volume of a material particle can be given by

$$V_p = \int_{\Omega_p} \chi_p \mathrm{d}\Omega. \tag{15}$$

For a granular material with stationary freezing point, the semi-discrete equations at node I read

$$\sum_J C_{IJ} T_{J,t} = Q_I^{\text{ext}} + Q_I^{\text{int}}, \tag{16}$$

$$\sum_J M_{IJ} a_{iJ} = f_{iI}^{\text{ext}} + f_{iI}^{\text{int}}, \tag{17}$$

with

$$C_{IJ} = \sum_p m_p c_p \phi_{Ip} N_{Jp}, \tag{18}$$

$$M_{IJ} = \sum_p m_p \phi_{Ip} \phi_{Jp}, \tag{19}$$

$$Q_I^{\text{ext}} = \sum_p V_p \phi_{Ip} (Q_{tp} + L \rho_s \theta_{sp,t}) + \sum_p \bar{q}_p h^{-1} \phi_{Ip}, \tag{20}$$

$$Q_I^{\text{int}} = \sum_p V_p \phi_{Ip,i} k_{pij} T_{p,j}, \tag{21}$$

$$f_{iI}^{\text{ext}} = \sum_p m_p \phi_{Ip} b_{ip} + \sum_p m_p \phi_{Ip} \bar{t}_{ip} h^{-1}, \tag{22}$$

$$f_{iI}^{\text{int}} = -\sum_p V_p \phi_{Ip,j} \sigma_{pij}, \tag{23}$$

where C and M are the consistent heat capacity matrix and mass matrix, respectively; Q and f_i are heat and mechanical loads, respectively (the superscripts "int" and "ext" denote internal and external loads, respectively); h is the virtual boundary layer thickness serving for the boundary integration [22]; m_p is the mass of particle p; ϕ_{Ip} and $\phi_{Ip,i}$ are the weighting and gradient weighting functions, respectively, defined as

$$\phi_{Ip} = \frac{1}{V_p} \int_{\Omega_p} \chi_p N_I \mathrm{d}\Omega, \tag{24}$$

$$\phi_{Ip,i} = \frac{1}{V_p} \int_{\Omega_p} \chi_p N_{I,i} \mathrm{d}\Omega. \tag{25}$$

To facilitate the computation, the scheme of lumped matrix is employed, i.e.,

$$C_I = \sum_p m_p c_p \phi_{Ip}, \quad M_I = \sum_p m_p \phi_{Ip}, \tag{26}$$

such that

$$C_I T_{I,t} = Q_I^{\text{ext}} + Q_I^{\text{int}}, \quad M_I a_{iI} = f_{iI}^{\text{ext}} + f_{iI}^{\text{int}}. \tag{27}$$

For a material point subject to phase transition with stationary freezing temperature, the rate of volumetric fraction of ice is given by

$$\theta_{sp,t} = -\frac{k_{pij} T_{p,j}}{L \rho_s}. \tag{28}$$

3.3 Temporal discretization

The Euler forward method is adopted to solve the semi-discrete equations in Eq. (27) in an explicit manner. Indeed, this explicit MPM in conjunction with the scheme of lumped matrix has been popular in the literature for its straightforward numerical implementation [23]. In this scheme, the discrete equations for nodal temperature and velocity are written as

$$T_I^{(t+\Delta t)} = T_I^{(t)} + T_{I,t}^{(t)} \Delta t, \tag{29}$$

$$v_{iI}^{(t+\Delta t)} = v_{iI}^{(t)} + a_{iI}^{(t)} \Delta t, \tag{30}$$

where the superscripts t and $t + \Delta t$ indicate the variables at the start and end of the processing timestep hereafter, respectively. For the mechanical part, the movement of material points can be solved according to the kinematic fields of the background grid. Two direct candidate methods are considered here, i.e., the so-called FLIP (fluid implicit particle [24]) method and PIC (particle in cell [25]) method, where particle velocity is updated as

$$v_{ip}^{(t+\Delta t)} = v_{ip}^{(t)} + \sum_I a_{iI}^{(t)} \phi_{Ip}^{(t)} \Delta t, \quad \text{for FLIP}, \tag{31}$$

$$v_{ip}^{(t+\Delta t)} = \sum_I v_{iI}^{(t)} \phi_{Ip}^{(t)} + \sum_I a_{iI}^{(t)} \phi_{Ip}^{(t)} \Delta t, \quad \text{for PIC}. \tag{32}$$

One major difference between the FLIP and PIC methods is that the FLIP method uses the grid accelerations only while the PIC method uses the updated grid velocities. Stomakhin et al. [26] suggested a combination of the FLIP and PIC methods by regrading PIC as a damping term as follows:

$$v_{ip}^{(t+\Delta t)} = v_{ip}^{(t)} + \sum_I a_{iI}^{(t)} \phi_{Ip}^{(t)} \Delta t - \alpha_{\text{PIC}} \left(v_{ip}^{(t)} - \sum_I v_{iI}^{(t)} \phi_{Ip}^{(t)} \right), \tag{33}$$

where $\alpha_{\text{PIC}} \in [0, 1]$ is the PIC fraction. With grid damping α_g and particle damping α_p, the damped particle velocity reads

$$v_{ip}^{(t+\Delta t)} = v_{ip}^{(t)} + \sum_I a_{iI}^{(t)} \phi_{Ip}^{(t)} \Delta t - (\alpha_{\text{PIC}} + \alpha_p) v_{ip}^{(t)}$$
$$+ (\alpha_{\text{PIC}} - \alpha_g) \sum_I v_{iI}^{(t)} \phi_{Ip}^{(t)}, \tag{34}$$

and the particle position is updated with a general second-order FLIP formulation [27]

$$x_{ip}^{(t+\Delta t)} = x_{ip}^{(t)} + \sum_I v_{iI}^{(t+\Delta t)} \phi_{Ip}^{(t)} \Delta t - \frac{\Delta t}{2} \Big[\sum_I a_{iI}^{(t)} \phi_{Ip}^{(t)} \Delta t$$
$$+ (\alpha_{\text{PIC}} + \alpha_p) v_{ip}^{(t)} + (\alpha_{\text{PIC}} - \alpha_g) \sum_I v_{iI}^{(t)} \phi_{Ip}^{(t)} \Big]. \tag{35}$$

Similar to the FLIP and PIC methods on velocity update in the mechanical part, two possible schemes can be formulated to update the particle temperature (direct one $T_p^{(t+\Delta t)}$ and remapped one $T_p'^{(t+\Delta t)}$), i.e.,

$$T_p^{(t+\Delta t)} = T_p^{(t)} + \sum_I \phi_{Ip}^{(t)} T_{I,t}^{(t)} \Delta t, \tag{36}$$

$$T_p'^{(t+\Delta t)} = \sum_I \phi_{Ip}^{(t)} T_I^{(t+\Delta t)}. \tag{37}$$

The direct particle temperature $T_p^{(t+\Delta t)}$ is then mapped to nodes for updating nodal temperature $T_I^{(t+\Delta t)}$. However, $T_p^{(t+\Delta t)}$ has inevitable oscillations like stress at material points due to an intrinsic numerical issue in MPM, as reported in a previous study [28]. Hence, a remapping of nodal temperature, i.e., remapped particle temperature $T_p'^{(t+\Delta t)}$, is employed to obtain smooth particle temperature, which then serves as an input for the RVEs.

The phase state update follows the particle temperature update. This framework applies a two-phase update scheme for coarse soils (e.g., sands) and fine soils (e.g., silts), respectively, due to the significantly different freezing behaviors between coarse and fine soils. Moreover, only the volume fraction update of ice is presented here, and its water counterpart can be obtained in terms of a saturation condition. Note that rather than updating the ice volume fraction using $\theta_{sp,t}$ directly, an equivalent heat capacity is introduced to relate latent heat with temperature, leading to Eq. (A2) by substituting Eq. (28) (see Appendix A) into Eq. (9). As a consequence, the ice volume fraction is updated with the assistance of the updated particle temperature acquired by Eq. (A2).

The freezing/thawing curve for coarse soils is depicted by such a step function of particle temperature as

$$S_f^{t+\Delta t} = \begin{cases} 1, & \text{if } T_p^{t+\Delta t} \geqslant T_0, \\ (T_p^{t+\Delta t} - T_{\text{res}})/(T_0 - T_{\text{res}}), & \text{if } T_{\text{res}} \leqslant T_p^{t+\Delta t} < T_0, \\ 0, & \text{if } T_p^{t+\Delta t} < T_{\text{res}}, \end{cases} \tag{38}$$

with the ice volume fraction updated by

$$\theta_s^{t+\Delta t} = n(1 - S_f^{t+\Delta t}), \tag{39}$$

where T_0 and T_{res} are the freezing point of soils and the residual freezing temperature (ice starts freezing at T_{res}), respectively. Note that a sufficiently small T_{res} (e.g., $-0.1\,°\text{C}$) is introduced to facilitate numerical implementation with respect to $T_0 = 0\,°\text{C}$.

As for fine soils, in the presence of mineral solutes, the freezing point is temperature-dependent during phase transition. Hence, the unfrozen water content is introduced by an empirical equation as denoted in Eq. (A1). Thus, the ice volume fraction θ_s can be solved by combining Eqs. (4) and (A1), i.e.,

$$\theta_s^{t+\Delta t} = n - \frac{\rho_g}{\rho_f}(1 - n)\Big[\bar{w} + (w_0 - \bar{w})\mathrm{e}^{a(T_p^{t+\Delta t} - T_0)}\Big]. \tag{40}$$

One may prefer to identify the soil unfrozen curve using water saturation instead of water content. The saturation-wise ice volume fraction update is given by

$$\theta_s^{t+\Delta t} = n - (S_{f0} - S_{\text{fres}})e^{-\frac{(T_p^{t+\Delta t}-T_0)^2}{a}} + S_{\text{fres}}, \quad (41)$$

where S_f, S_{f0} and S_{fres} are the current water saturation, water saturation at the freezing point and the unfrozen water saturation, respectively; a can also be regarded as a parameter that determines the shape of unfrozen curve of soil as that introduced in Eq. (A1) in Appendix.

To ensure numerical stability and convergence in the proposed staggered coupling algorithm, the mechanical timestep is constrained by the propagation speed of elastic waves, and the thermal timestep satisfies the CFL condition [11,28], i.e.,

$$\Delta t < \frac{l_e}{\sqrt{E/\rho}}, \quad \text{for mechanical}, \quad (42)$$

$$\Delta t < \frac{l_e^2 \rho c}{bk}, \quad \text{for thermal}, \quad (43)$$

where E is Young's modulus of an RVE packing; b is an adjustable factor, with a default value of 1; l_e is the minimum element size of a mesh; k is the mean thermal conductivity, i.e., average of the diagonal terms of the thermal conductivity tensor k_{ij}.

4. Multiscale framework: DEMPM

4.1 Homogenization of DEM RVE

In the proposed multiscale framework, the RVE-scale response of a granular material is modeled using DEM. Following previous studies [12, 13, 29], a DEM RVE is configured with a parallelepiped-shaped cell with periodic boundary conditions. Figure 2 illustrates an RVE cell and its periodic neighbor images in two-dimensional (2D).

As commonly implemented in continuum mechanics, both Eulerian (x_i) and Lagrangian (X_i) coordinates can be employed to describe the deformation of an RVE cell such that

$$x_i = H_{ij}X_j, \quad (44a)$$
$$X_j = H_{jk}^{-1}x_k, \quad (44b)$$

where H_{ij} is the deformation (gradient) tensor with the cell basis vectors as its columns, and H_{ij}^{-1} is its inverse. Therefore, the material time derivative for Eq. (44a) is given as

$$\dot{x}_i = \underbrace{\dot{H}_{ij}X_j}_{v_{hi}} + \underbrace{H_{ij}\dot{X}_j}_{v_{fi}}, \quad (45)$$

where v_{fi} and v_{hi} are the non-affine and affine velocities, respectively. Note that v_{fi} is also referred to as the fluctuating
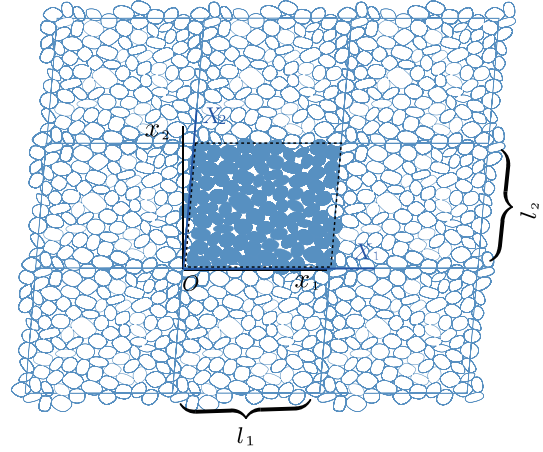
Figure 2 An illustration of a periodic cell for an RVE assembly.

velocity resulting from the resultant force, while v_{hi} is attributed to the homogeneous deformation of the RVE cell, given by

$$v_{hi} = L_{ij}x_j, \quad (46a)$$
$$L_{ij} = \dot{H}_{ik}H_{kj}^{-1}, \quad (46b)$$

where L_{ij} is the velocity gradient tensor of the cell deformation, which is prescribed when loading an RVE in the proposed framework.

Considering the fact that an RVE deforms in terms of strain-controlled incremental loading and its deformation is sufficiently small during each time step of DEM, the deformation can be homogenized by such a strain tensor ε_{ij} of the periodic cell (RVE) that

$$\varepsilon_{ij} = \frac{1}{2}(H'_{ij} + H'_{ji}) - \delta_{ij}, \quad (47)$$

where H'_{ij} is the deformation gradient tensor with respect to the reference configuration. Therefore, the volumetric strain ε_v and the deviatoric strain ε_q read

$$\varepsilon_v = \varepsilon_{ii}, \quad (48a)$$

$$\varepsilon_q = \sqrt{\frac{2}{3^{n-2}}\varepsilon'_{ij}\varepsilon'_{ij}}, \quad n = 2 \text{ (2D) or 3 (3D)}, \quad (48b)$$

where ε'_{ij} is the deviatoric strain tensor, $\varepsilon'_{ij} = \varepsilon_{ij} - \frac{1}{n}\varepsilon_v\delta_{ij}$.

The homogenized stress tensor σ_{ij} within an RVE assembly can be expressed from contact forces and fluctuating velocities of particles [30,31], i.e.,

$$\sigma_{ij} = \frac{1}{V}\sum_{c\in V}f_i^c b_j^c + \frac{1}{V}\sum_{p'\in V}m_{p'}v_{fi}^{p'}v_{fj}^{p'}, \quad (49)$$

where V is the volume of the assembly; f_i^c and b_j^c are the contact force and the branch vector, respectively; $m_{p'}$ is the mass of particle p'. It is worth noting that the contact force-related

term denotes stress transmission through contact force networks, whereas the fluctuating velocity-related term reflects the kinetic stress associated to the momenta transferred by particles. In general, compared with the contact force-related term, the fluctuating velocity-related term is negligibly small.

4.2 Bridging the continuum and RVE scales

The idea of hierarchical multiscale modeling [12-14] can be extended to model the thermo-mechanical responses of granular media. In our previous study [14], DEM-simulated RVEs have been introduced to couple with FEM for modeling thermo-mechanical responses of granular media. Replacing FEM with MPM at the continuum scale, a new framework DEMPM is proposed to model the freeze and thaw behaviors of granular media as illustrated in Fig. 3, where thawing-induced large deformation can be captured with our newly proposed phase-transition models at both RVE and continuum scales. Specifically, thermal transfer through the continuum modeled by material points changes the volumetric fraction of ice, thereby influencing the inter-particle bond strength of RVEs modeled by DEM. Stress and deforma-

tion of each material point are tracked by a corresponding RVE, bypassing the need for assuming phenomenological constitutive models in MPM. Interested readers are referred to our previous work on hierarchical multiscale modeling. In the proposed DEMPM framework, the DEM solver is much more computationally intensive than the MPM one. Hence, a thread-block-wise approach [29] is employed to accelerate RVE DEM simulations on GPUs.

5. Verification, validation and example

5.1 Biaxial compression

5.1.1 Unfrozen granular media

Biaxial compression is simulated to verify the implementation of the mechanical component of the proposed framework. With the basic parameters outlined in Table 1, three RVE packings with void ratios of 0.161 (dense), 0.203 (medium dense) and 0.235 (loose) are prepared under an isotropic confining stress of 100 kPa. Figure 4a-c shows the
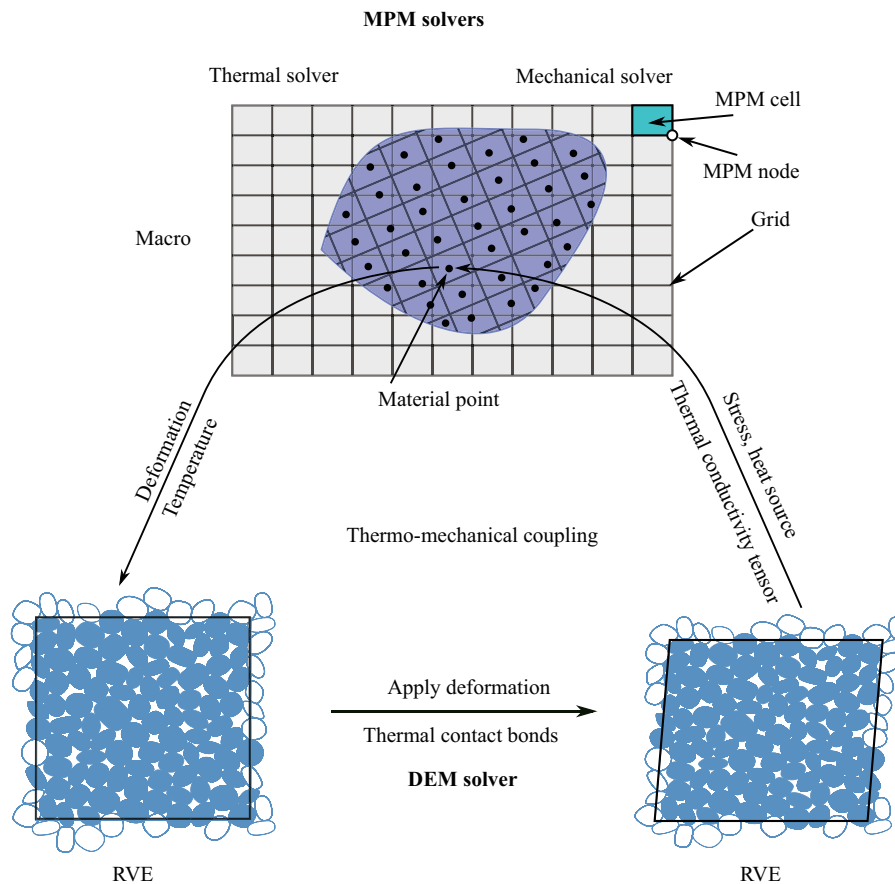
Figure 3 Multiscale framework for thermo-mechanical modeling by coupling MPM and DEM.

Table 1   Basic parameters for DEM RVEs

Parameter	Value
Particle number	400
Particle size r (mm)	2.5-5.0
Material density ρ (kg/m^3)	2650
Inter-particle contact stiffness k_n, k_t (N/m)	1×10^6
Inter-particle coefficient of friction μ	0.5
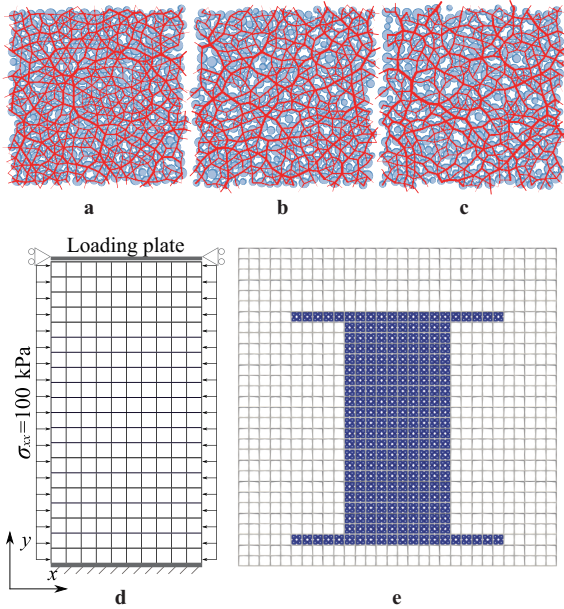
Figure 4   Initial RVE packings with contact force networks: **a** dense, **b** medium dense and **c** loose; simulation setup of biaxial test: **d** loading condition, **e** material points and background grid.

snapshots of the three packings, respectively, where isotropic contact force networks suggest an initially isotropic stress state. A 1 m × 2 m granular column is meshed into 10×20 cells with 4 material points per cell. Figure 4d illustrates the loading setup, where the column is fixed at the bottom and loaded by moving the top plate downward in 0.02 m/s, while a constant confining stress of 100 kPa is maintained at both sides. The whole MPM model is shown in Fig. 4e. The timesteps for MPM and DEM are 1×10^{-3} s and 1×10^{-5} s, respectively.

Figure 5 shows contours of equivalent shear strain within the three numerical specimens at an axial strain of 20%. It can be seen that strain localization identified by shear band is more remarkable with decreasing initial void ratio, which is in agreement with the general observation on mechanical behavior of sands in laboratory. Moreover, stress-strain curves change from strain-hardening to strain-softening pattern when decreasing initial void ratio as shown in Fig. 6, and both residual axial stress and volumetric strain reach critical values. Such mechanical responses have been well documented in soil mechanics [32].

5.1.2   Frozen granular media

Frozen granular media may have different volumetric fractions of ice that control their overall strength. The breakage strength coefficient β_b introduced in the contact bond model can capture the influence of volumetric fraction of ice. For simplicity, three simulations are conducted with different bond breakage strength coefficient of $\beta_b = 1.0$, 2.0 and 3.0, respectively, where the normal and shear bond strengths c_n and c_t are set to 10 MPa. Following the simulation setup in Sect. 5.1.1, biaxial compression is performed on the medium dense specimen, where inter-particle bonds are active at all contacts prior to loading. Figure 7 shows contours of equivalent shear strain at the final states. It can be seen that shear strain localizes into a single band with increasing contact bond strength. Moreover, the contact bond strength augments the overall strength of specimens as shown in Fig. 8, where
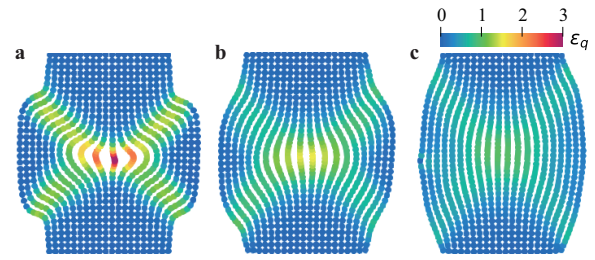
Figure 5   Final states with contours of equivalent shear strain: **a** dense, **b** medium dense and **c** loose.
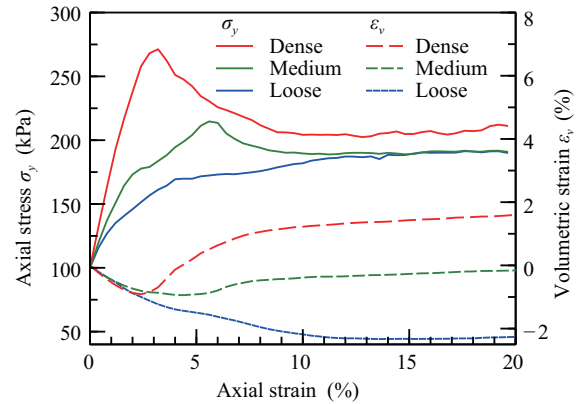
Figure 6   Evolution of axial stress σ_y and volumetric strain ε_v for different initial densities during biaxial compression.
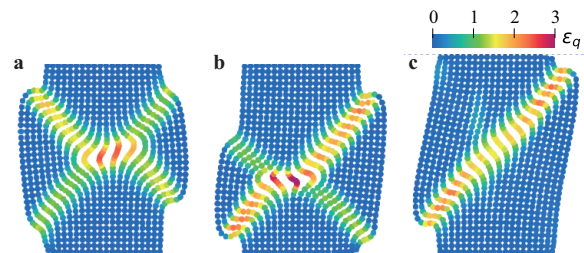
Figure 7   Final states with contours of equivalent shear strain: **a** $\beta_b = 1.0$, **b** $\beta_b = 2.0$ and **c** $\beta_b = 3.0$. Note: axial strain is 16% in **c**.
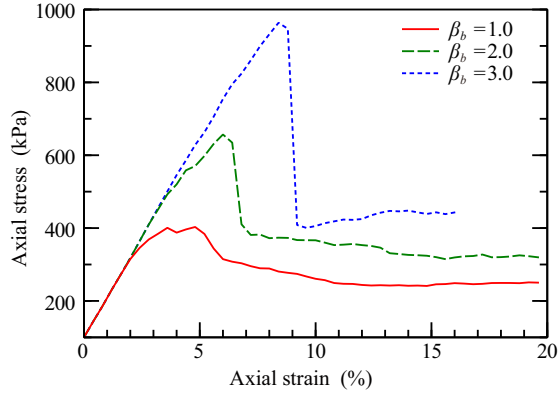
Figure 8　Stress-strain curves for different bond strengths during biaxial compression.

a sharper drop of axial stress is observed due to bond break-age for higher bond strength. These numerical observations are qualitatively in agreement with the experimental one for cemented sands [33] or hydrate-bearing sands [34].

5.2　Column collapse of soils

To validate the multiscale framework, a column collapse test is simulated and calibrated against the experimental result reported in the literature. Following the experimental settings in Ref. [35], a 0.2 m × 0.1 m rectangular column of soils is set up as shown in Fig. 9a . The entire column is meshed into 40 × 20 elements (cells) composed of 3200 material points (4 material points per cell). Three rigid walls are employed to confine the soil column, where the left rigid wall and the outlet baffle only constrain the horizontal displacement, and the base wall fixes the vertical displacement with additional friction condition ($\mu = 0.15$ is tuned). DEM RVE packings are prepared with the same basic parameters listed in Table 1 except that friction coefficient is now tuned to 0.45. Once the material points are generated, a geostatic process is performed to ensure an initial stress field induced by gravity, where artificial dampings (particle damping of 0.2 and PIC fraction of 1.0) are applied to accelerate the simulation process. After that, the column collapse is triggered by suddenly removing the outlet baffle, and certain dampings (particle damping and PIC fraction are 0.05 and grid damping is 0) are prescribed to facilitate the numerical stability for the dynamic problem.

Figure 9b demonstrates a comparison between the experimental and numerical results. Removing the outlet baffle leads to large deformation of the material points, where the soil column collapses and slides to form a relative stable slope. The black circles and diamonds indicate the surface profile and the failure line from the experimental result [35], respectively. It can be observed that the numerical result is

consistent with the experimental one, indicating that the proposed multiscale framework performs well for large deformation problems.

5.3　Heat transfer with phase transition

Soil experiencing freezing and thawing process may exhibit significantly different mechanical and thermal responses due to their granular configuration. The freezing process for granular soils (e.g., sand) is called as *in situ*, and the phase transition of the moisture ends at pore ice. Nevertheless, the soil composed of fine particles (e.g., silt and clay) indicates a slow ice growth compared to the freezing front moving as a result of the unfrozen moisture [5]. This section verifies the MPM implementation of the heat transfer model involving phase transition for both coarse and fine grains. Cases of thawing-front propagation in pure ice and porous soil are used to demonstrate the robustness of this framework.

5.3.1　One-dimensional problems

(1) Thawing front propagation in coarse soils (pure ice)
　　Stefan problems [36, 37] refer to the solution of the movement of a freezing or thawing front. Among different forms of the Stefan solution reported in Ref. [38], the solution of thawing front propagation within ice is selected as a benchmark. Given a soil column with a porosity of $n = 1$, it is fully saturated by pore-filling ice under an ambient temperature of $T_0 = 0\,^{\circ}\mathrm{C}$ as shown in Fig. 10a. The left boundary is prescribed with a constant temperature ($T_{\mathrm{BC}} = 1\,^{\circ}\mathrm{C}$) to generate a thawing front. The analytical Stefan solution under the steady-state assumption gives the relationship between the thawing front and time as

$$X = \sqrt{\frac{2\lambda T_s}{S_{wf}\rho_w \varepsilon L_f}t}, \tag{50}$$

where λ is heat conductivity; T_s is the temperature boundary condition of the thawing front; S_{wf} is the water saturation in thawed zone; ρ_w is the water density; ε is the soil porosity and L_f is the latent heat per unit mass.

　　According to the Stefan solution, the material properties are listed as follows. The specific heat capacity of the ice and water are defined as $c_f = c_s = 0.1\,\mathrm{J/(kg\,K)}$ to ensure a quasi-steady heat transfer state. The heat conductivity is set as $\lambda = k_f = k_s = 0.1\,\mathrm{W/(m\,K)}$ to allow a larger time step. All the other properties such as density, soil porosity, soil saturation and latent heat of fusion per unit mass are assumed to be units for simplification.

　　Figure 10b shows the evolution of the thawing front obtained from this study (red circles) and the Stefan solution (blue line). It demonstrates a good agreement of the result
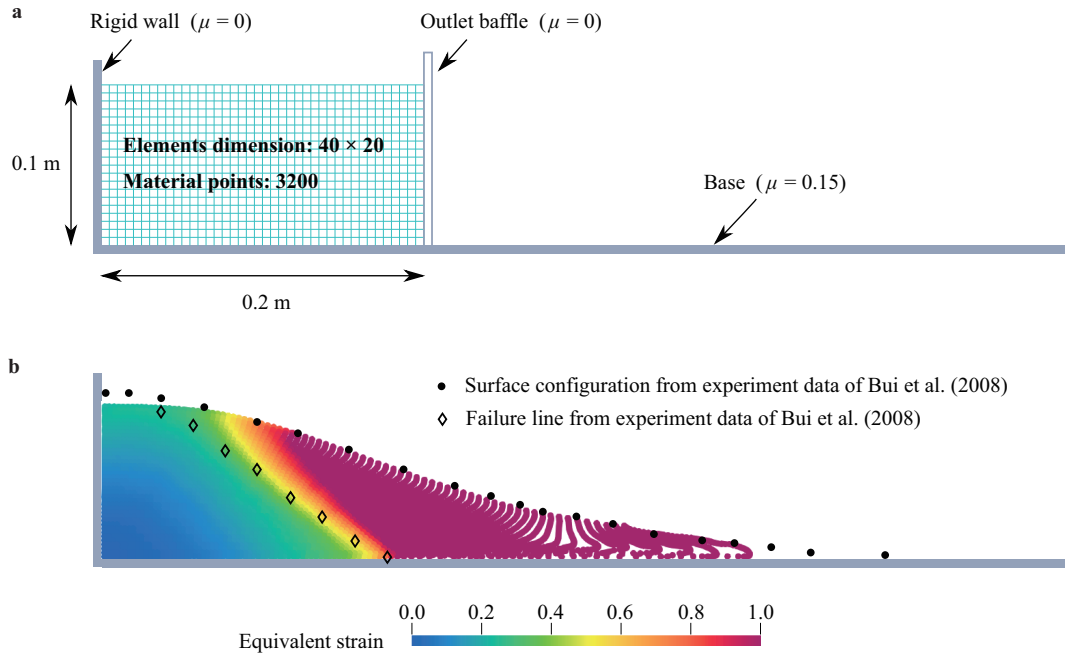
Figure 9   Column collapse simulation: (a) geometry configuration, and (b) comparison between experimental and numerical results.

matching. A slight difference between these two results can be observed when the time exceeds 8 s, which may be attributed to the iteration scheme in MPM. Specifically, the heat transfer model is implemented explicitly in a dynamic manner, while the analytical solution assumes a steady state. Moreover, the transient specific heat term in Eq. (10) accounts for the result deviation, and results are expected to match better for sufficiently small specific heat.

(2) Freezing front propagation in fine soils

All the geometry and material settings except the ice density for this problem are identical to that of Ref. [39] as shown in Fig. 11a. The density of soil ρ_g = 2650 kg/m^3, the density of water and ice $\rho_f = \rho_s$ = 1000 kg/m^3. The specific heat capacities of soil, water and ice are set to be 900, 4180 and 2100 J/(kg K). The thermal conductivities of soil, water and ice are as 2.92, 0.56 and 2.24 W/(m K). The latent heat of fusion per unit mass of water is 3.33×10^5 J/kg. The soil has an initial temperature of (T_0 = 5 °C) and fixed boundary conditions in temperature: the left boundary (T_{BC1} = −5 °C) and the right boundary (T_{BC2} = 5 °C). Note that the material composition and the material properties applied here are different from that in the first case. The saturated soil (instead
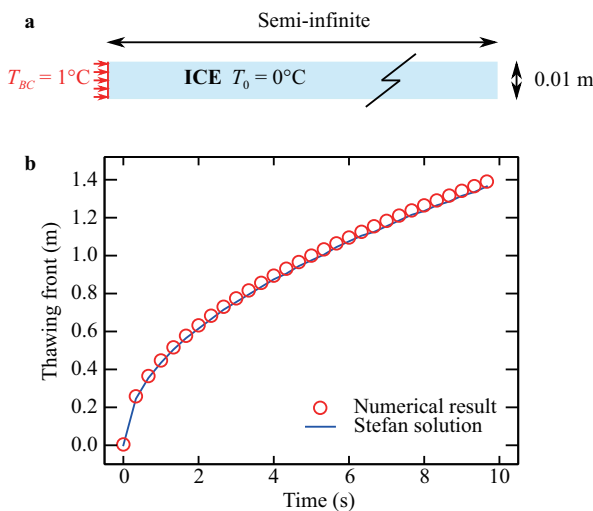
Figure 10   **a** Model domain and boundary condition for the thawing front propagation within ice. **b** Thawing front displacement as a function of time from results of this study and Stefan solution.
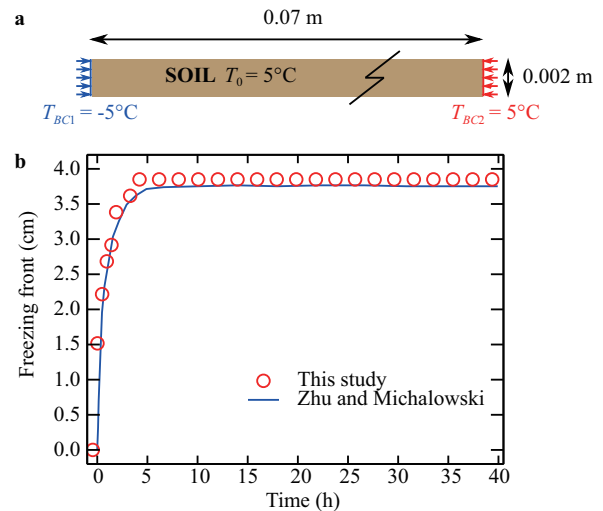
Figure 11   **a** Model domain and boundary condition for the freezing front propagation within porous soil. **b** Freezing front displacement as a function of time from results of this study and Zhu and Michalowski [39].

of pure ice) has a porosity of $n = 0.427$ that corresponds to an unfrozen water content of $w_0 = 0.285$. The material properties are weighted from the soil and water matrix according to the mixture theory, referring to Sect. 2.2, and the unfrozen water content follows a non-linear relation with temperature that can be empirically given by Eq. (A1).

The evolution of freezing front is shown in Fig. 11b. It can be seen that frozen front propagation displacement increases sharply at the initial stage of simulation, but it can reach a critical state after 6 h. On the whole, our simulated freezing front propagation in MPM agrees well with that from FEM/Abaqus in Ref. [39].

5.3.2 2D problem

Frozen inclusion thaw [40] problem is used to verify the framework for 2D solution as shown in Fig. 12a. The geometry and material parameters adopted in this benchmark inherit that from Ref. [40]. The density of soil $\rho_g = 2650$ kg/m^3, the density of water and ice $\rho_f = \rho_s = 1000$ kg/m^3. The specific heat capacities of soil, water and ice are set to

be 835, 4182 and 2060 J/(kg K). The thermal conductivities of soil, water and ice are as 9, 0.6 and 2.14 W/(m K). The latent heat of fusion per unit mass of water is 3.34×10^5 J/kg. The solution domain is assigned with an initial temperature condition ($T_0^+ = 5\,°C$) except the blue square initialized with $T_0^- = -5\,°C$. An inflow thermal boundary is imposed on the left side, $T_{BC} = 5\,°C$. The saturated soil has a porosity of $n = 0.37$, and the unfrozen water content indicates a non-linear dependency on the temperature as suggested by Ref. [41].

Figure 12b shows the contour of temperature at $t \approx 6.4$ h. Despite being squarely initialized at the frozen region, the temperature distributes isotropically around the frozen center. Quantitatively, the temperature profile along the middle axis is plotted together with the results from Ref. [40] in Fig. 12c. The temperature changes sharply near the center of the frozen region and shows a flatter tendency at $t = 1260$ s. With heat transfer, the temperature valley moves upwards, and the temperature profile becomes asymmetric due to the influence of boundary conditions ($t = 5.9$ d). Our simulated results match well with that of Ref. [40], demonstrating the predictive capability of our model for capturing the thawing front propagation.
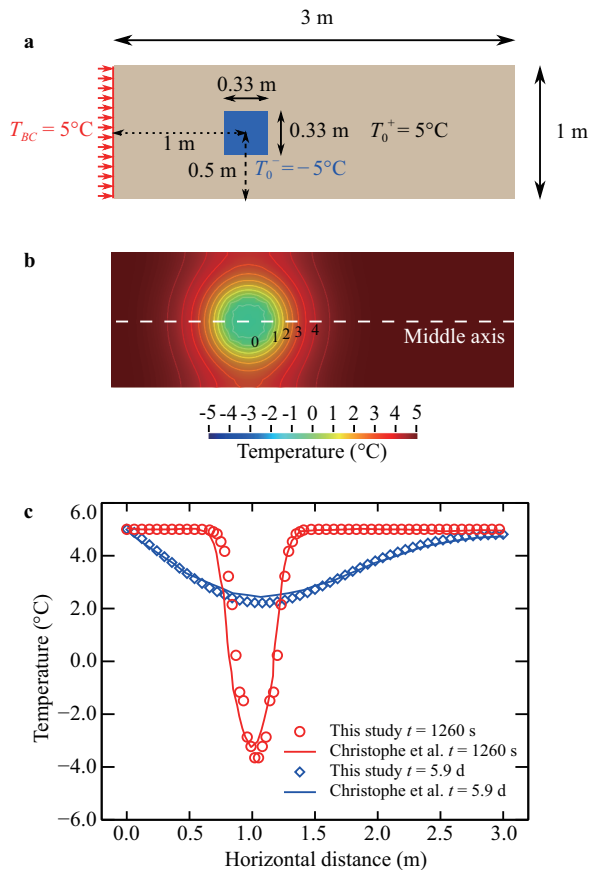
5.4 Example: thawing-induced slope sliding

After verification and validation, the proposed framework is further applied to thawing-induced slope sliding to showcase its capability of modeling engineering-scale problems. Figure 13a shows the geometrical configuration of the slope with a height of 10 m and inclined angle of 45°. The base dimension is set as 40 m (width) × 4 m (height) to eliminate the potential boundary effect from the ground. The entire domain has a uniform background grid with a cell size of 0.25 m. The slope and base are discretized into 20203 material points with four per cell. Roller displacement boundary condition is applied on both left and right sides to fix the horizontal displacement, while all the degrees of freedom are constrained for the bottom boundary. The soil is assumed uniformly frozen at an ambient temperature of $T_0 = -5\,°C$. The blue line around the slope outline illustrates the thermal boundary condition ($T_{BC1} = -5\,°C$), which characterizes the semi-infinite frozen soil and avoids the temperature localization due to the adiabatic boundary. A heat source (red line) with constant temperature ($T_{BC2} = 50\,°C$) is introduced to simulate a heater in a borehole, which mimics the heating method in gas-hydrate exploitation.

The basic mechanical properties adopt the same as that in Table 1, and the contact bond strength c_n and c_t are set to 3.2 MPa to model a slope with poor initial mechanical performance. The other material properties related to phase transi-

Figure 12 **a** Model domain and boundary condition for the frozen inclusion thaw within porous soil. **b** Contour of temperature field. **c** The temperature distribution along the middle axis of the solution domain from this study and Grenier et al. [40].
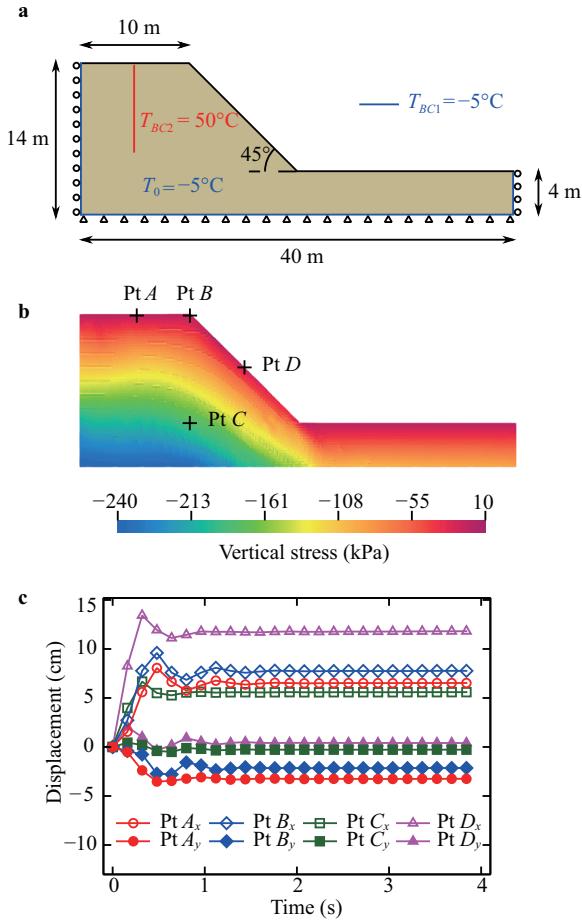
Figure 13 **a** Geometrical and boundary condition configuration of the slope. **b** Vertical stress (position for tension) distribution of the slope after the geostatic process and four probed points. **c** Vertical and horizontal displacement as a function of time for probed points.

tion are selected as follows: the density of soil $\rho_g = 2650\,\mathrm{kg/m^3}$, the density of water and ice $\rho_f = \rho_s = 1000\,\mathrm{kg/m^3}$ (the density difference between ice and water is neglected in this simulation), the initial porosity $n = 0.43$. Following Ref. [15], specific heat capacities of soil grain c_g, ice c_s and water c_f are set to be 900, 2100 and 4180 J/(kg K), respectively, and the thermal conductivities of soil k_g, ice k_s and water k_f are 2.92, 2.24 and 0.56 W/(m K), respectively. It is worth noting that the critical MPM time step for heat transfer is much larger than that for mechanical response for the given real material properties of soils. To facilitate speeding up a practical simulation, the thermal conductivity is scaled up by a factor of 86400 so that a simulated time of 1 s corresponds to 1 day for heat transfer in the real world. Such a scaling scheme has also been employed in the literature, e.g., Ref. [11]. The time step is set to 0.001 s.

The geo-static process is performed with the temperature boundary T_{BC2} disabled, following a protocol depicted as follows. First, bond-free RVEs are prepared with different initial stress states in terms of the vertical position of the corre-

sponding material points. Next, the entire model is subjected to a gravitational acceleration of 0.5 g. Once the kinematic energy ratio meets the specific threshold ($E_k/E_g < 10^{-4}$), the contact bonds are activated in conjunction with a full gravity loading of 1 g to form the final geo-static stress field shown in Fig. 13b. Damping of particle, grid and PIC fraction are all set to 1 to ensure a quasi-static geo-static process. Note that the positive geo-static stress denotes tension undertaken by contact bonds. Moreover, the displacement variations of four points Pt A, B, C and D highlighted in Fig. 13b are probed in Fig. 13c to intuitively ensure a stable slope after the geo-static process. It can be seen that all probed points become relatively stable at about 1 s, indicating that the final slope is sufficiently stable under gravity.

The thawing process begins at a new time instant $t = 0$ s when the temperature boundary T_{BC2} is activated. Figure 14 shows the evolution of contours of temperature, normalized ice fraction and equivalent strain at different simulation time instants of $t = 20$ s, 76 s, 78 s, 80 s and 82 s that correspond to heating of 20 days, 76 days, 78 days, 80 days and 82 days, respectively. It can be seen that the thawing process is rather slow and lasts about 78 days ($t = 78$ s in simulation time) until a sudden sliding is triggered. The sliding is so quick that the change is negligibly small in both temperature and normalized ice fraction (Fig. 14a and b), which suggests an accumulative effect of thawing process on the slope stability. Indeed, strain localization becomes stronger before the sudden sliding, referring to the sliding arc identified by the equivalent strain in Fig. 14c.

The sudden failure pattern of slope simulated here is critical in engineering practices, which may trigger earthquakes and tsunamis in submarine settings during the exploitation of gas hydrates [3]. Bypassing the phenomenological conventional constitutive model, the proposed framework is demonstrated to be capable of capturing thawing-induced sliding well in granular media, which can be further applied to investigate the mechanism of thawing-induced sliding from a multiscale perspective.

6. Summary

A hierarchical multiscale modeling framework is proposed to model freeze-thaw behavior in granular media, in which DEM-simulated freeze-thaw responses of RVEs serves as constitutive relations for solving initial and boundary value problems in MPM. In the proposed framework, phase transition of pore-filling materials (typically ice and water) within granular media is fully considered at both RVE and continuum scales so that heat transfer can be accurately captured during freezing or thawing. The framework is verified and
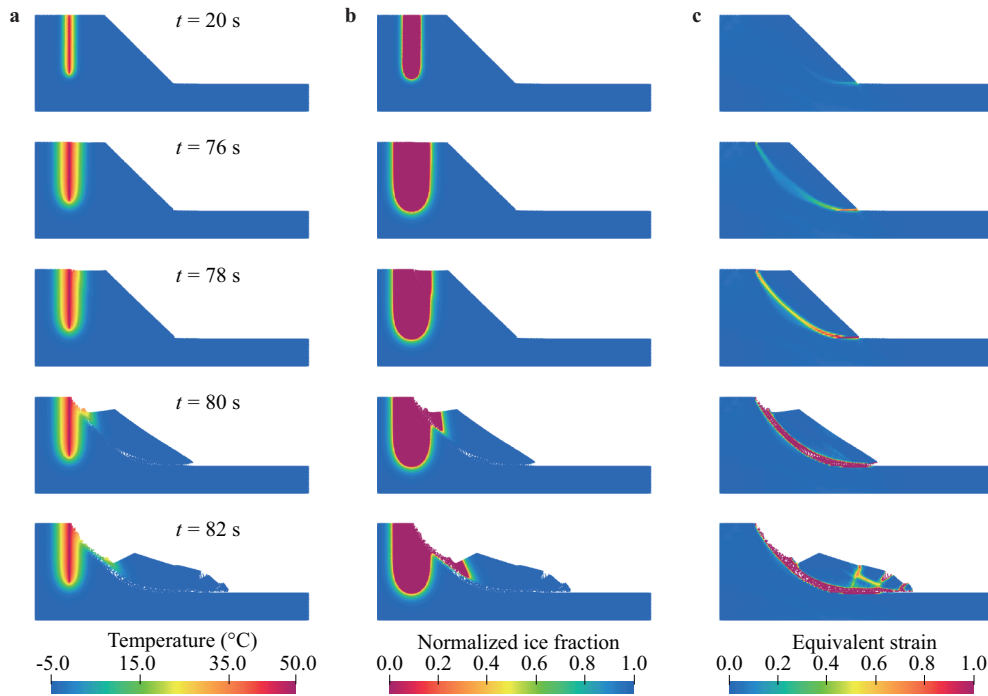
Figure 14 Contours of **a** temperature, **b** normalized ice fraction and **c** equivalent strain at different time instants during thawing.

validated against analytical and experimental results via a set of simulations including biaxial compression, column collapse, and heat transfer within coarse and fine soils. As a showcase of potential engineering-scale applications, we further use the developed model to simulate thawing-induced slope sliding triggered by heating in a borehole, which mimics the exploitation of gas hydrates. It demonstrates that the proposed framework is effective and robust in capturing engineering-scale freeze-thaw behavior of granular media.

Nevertheless, it requires further efforts to advance the framework. One possible improvement is to comprehensively model hydraulic effect and heat convection due to fluid flow that may play an important role in certain engineering problems.

1 A. I. Patton, S. L. Rathburn, and D. M. Capps, Landslide response to climate change in permafrost regions, Geomorphology **340**, 116 (2019).
2 N. Froitzheim, J. Majka, and D. Zastrozhnov, Methane release from carbonate rock formations in the Siberian permafrost area during and after the 2020 heat wave, Proc. Natl. Acad. Sci. USA. **118**, e2107632118 (2021).
3 M. Maslin, M. Owen, R. Betts, S. Day, T. Dunkley Jones, and A. Ridgwell, Gas hydrates: Past and future geohazard? Phil. Trans. R. Soc. A. **368**, 2369 (2010).
4 R. L. Michalowski, A constitutive model of saturated soils for frost heave simulations, Cold Regions Sci. Tech. **22**, 47 (1993).
5 R. L. Michalowski, and M. Zhu, Frost heave modelling using porosity rate function, Int. J. Numer. Anal. Meth. Geomech. **30**, 703 (2006).
6 S. Nishimura, A. Gens, S. Olivella, and R. J. Jardine, THM-coupled finite element analysis of frozen soil: Formulation and application, Géotechnique **59**, 159 (2009).
7 W. Cui, D. M. Potts, L. Zdravković, K. A. Gawecka, and D. M. G. Taborda, An alternative coupled thermo-hydro-mechanical finite element formulation for fully saturated soils, Comput. Geotech. **94**, 22 (2018).
8 M. Kardani, M. Nazem, D. Sheng, and J. P. Carter, Large deformation analysis of geomechanics problems by a combined rh-adaptive finite element method, Comput. Geotech. **49**, 90 (2013).
9 S. G. Bardenhagen, and E. M. Kober, The generalized interpolation material point method, Comput. Model. Eng. Sci. **5**, 477 (2004).
10 K. Soga, E. Alonso, A. Yerro, K. Kumar, and S. Bandara, Trends in large-deformation analysis of landslide mass movements with particular emphasis on the material point method, Géotechnique **66**, 248 (2016).
11 X. Lei, S. He, A. Abed, X. Chen, Z. Yang, and Y. Wu, A generalized interpolation material point method for modelling coupled thermo-hydro-mechanical problems, Comput. Methods Appl. Mech. Eng. **386**, 114080 (2021).
12 N. Guo, and J. Zhao, A coupled FEM/DEM approach for hierarchical multiscale modelling of granular media, Int. J. Numer. Meth. Eng. **99**, 789 (2014).

13 W. Liang, and J. Zhao, Multiscale modeling of large deformation in geomechanics, Int. J. Numer. Anal. Methods Geomech. **43**, 1080 (2019).

14 S. Zhao, J. Zhao, and Y. Lai, Multiscale modeling of thermo-mechanical responses of granular materials: A hierarchical continuum-discrete coupling approach, Comput. Methods Appl. Mech. Eng. **367**, 113100 (2020).

15 Y. Zhang, and R. L. Michalowski, Thermal-hydro-mechanical analysis of frost heave and thaw settlement, J. Geotech. Geoenviron. Eng. **141**, 04015027 (2015).

16 P. A. Cundall, and O. D. L. Strack, A discrete numerical model for granular assemblies, Géotechnique **29**, 47 (1979).

17 N. J. Brown, J. F. Chen, and J. Y. Ooi, A bond model for DEM simulation of cementitious materials and deformable structures, Granular Matter **16**, 299 (2014).

18 Z. Shen, M. Jiang, and C. Thornton, DEM simulation of bonded granular material. Part I: Contact model and application to cemented sand, Comput. Geotech. **75**, 192 (2016).

19 H. Wu, J. Zhao, and N. Guo, Multiscale insights into borehole instabilities in high-porosity sandstones, J. Geophys. Res. Solid Earth **123**, 3450 (2018).

20 H. Wu, N. Guo, and J. Zhao, Multiscale modeling and analysis of compaction bands in high-porosity sandstones, Acta Geotech. **13**, 575 (2018).

21 L. Onsager, Reciprocal relations in irreversible processes, I, Phys. Rev. **37**, 405 (1931).

22 D. Z. Zhang, X. Ma, and P. T. Giguere, Material point method enhanced by modified gradient of shape function, J. Comput. Phys. **230**, 6379 (2011).

23 A. de Vaucorbeil, V. P. Nguyen, S. Sinaie, and J. Y. Wu, Chapter two—Material point method after 25 years: Theory, implementation, and applications, Adv. Appl. Mech. **53**, 185 (2020).

24 J. U. Brackbill, and H. M. Ruppel, FLIP: A method for adaptively zoned, particle-in-cell calculations of fluid flows in two dimensions, J. Comput. Phys. **65**, 314 (1986).

25 F. H. Harlow, The particle-in-cell computing method for fluid dynamics, Methods Comput. Phys. **3**, 319 (1964).

26 A. Stomakhin, C. Schroeder, L. Chai, J. Teran, and A. Selle, A material point method for snow simulation, ACM Trans. Graph. **32**, 1 (2013).

27 J. A. Nairn, Numerical simulation of orthogonal cutting using the material point method, Eng. Fract. Mech. **149**, 262 (2015).

28 J. Tao, Y. Zheng, Z. Chen, and H. Zhang, Generalized interpolation material point method for coupled thermo-mechanical processes, Int.

J. Mech. Mater. Des. **12**, 577 (2016).

29 S. Zhao, J. Zhao, and W. Liang, A thread-block-wise computational framework for large-scale hierarchical continuum-discrete modeling of granular media, Int. J. Numer. Methods Eng. **122**, 579 (2021).

30 J. Christoffersen, M. M. Mehrabadi, and S. Nemat-Nasser, A micromechanical description of granular material behavior, J. Appl. Mech. **48**, 339 (1981).

31 F. Radjai, Multi-periodic boundary conditions and the contact dynamics method, Comptes Rendus Mécanique **346**, 263 (2018).

32 D. M. Wood, Soil Behaviour and Critical State Soil Mechanics (Cambridge University Press, Cambridge, 1990).

33 G. W. Clough, N. Sitar, R. C. Bachus, and N. S. Rad, Cemented sands under static loading, J. Geotech. Eng. Div. **107**, 799 (1981).

34 S. Kajiyama, M. Hyodo, Y. Nakata, N. Yoshimoto, Y. Wu, and A. Kato, Shear behaviour of methane hydrate bearing sand with various particle characteristics and fines, Soils Found. **57**, 176 (2017).

35 H. H. Bui, R. Fukagawa, K. Sako, and S. Ohno, Lagrangian meshfree particles method (SPH) for large deformation and failure flows of geomaterial using elastic-plastic soil constitutive model, Int. J. Numer. Anal. Meth. Geomech. **32**, 1537 (2008).

36 J. Stefan, Über die theorie der eisbildung, insbesondere über die eisbildung im polarmeere, Annalen der Physik **278**, 269 (1891).

37 S. L. Mitchell, and T. G. Myers, Application of standard and refined heat balance integral methods to one-dimensional Stefan problems, SIAM Rev. **52**, 57 (2010).

38 B. L. Kurylyk, J. M. McKenzie, K. T. B. MacQuarrie, and C. I. Voss, Analytical solutions for benchmarking cold regions subsurface water flow and energy transport models: One-dimensional soil thaw with conduction and advection, Adv. Water Resour. **70**, 172 (2014).

39 M. Zhu, and R. L. Michalowski, in Simulation of heat transfer in freezing soils using ABAQUS: Proceedings of ABAQUS Users' Conference, Stockholdm, 2005.

40 C. Grenier, H. Anbergen, V. Bense, Q. Chanzy, E. Coon, N. Collier, F. Costard, M. Ferry, A. Frampton, J. Frederick, J. Gonçalvés, J. Holmén, A. Jost, S. Kokh, B. Kurylyk, J. McKenzie, J. Molson, E. Mouche, L. Orgogozo, R. Pannetier, A. Riviére, N. Roux, W. Rühaak, J. Scheidegger, J. O. Selroos, R. Therrien, P. Vidstrand, and C. Voss, Groundwater flow and heat transport for systems undergoing freeze-thaw: Intercomparison of numerical simulators for 2D test cases, Adv. Water Resour. **114**, 196 (2018).

41 J. M. McKenzie, C. I. Voss, and D. I. Siegel, Groundwater flow with energy transport and water-ice phase change: Numerical simulations, benchmarks, and application to freezing in peat bogs, Adv. Water Resour. **30**, 966 (2007).

颗粒介质冻融行为的多尺度模拟

赵仕威, 陈昊, 赵吉东

摘要   本文提出了一种分阶多尺度建模范式来模拟颗粒介质中的冻融行为. 该多尺度方法分阶耦合了连续介质混合物理论与基于微观力学的均质化方法, 可以根据表征元(RVE)的离散元(DEM)解提取对应物质点的本构响应, 能够捕捉实际工程中典型的冻融过程. 具体地, 在表征元尺度上, 提出了考虑冻融过程对颗粒间接触强度影响的相变模型; 离散元模拟的表征元模型被嵌入到基于连续介质的物质点法(MPM)中, 以解决涉及冻融过程的初边值问题. 所提出的多尺度方法有效地实现了宏-微观尺度的桥接, 同时不再需要唯象连续本构模型. 该多尺度框架在经过校验后成功用于工程规模的热融滑坡模拟.